

REPORT DOCUMENTATION PAGE

Public reporting burden for this collection of information is estimated to average one hour per response, including the time for reviewing instructions, searching existing data sources, gathering and maintaining the data needed, and completing and reviewing the collection of information. Send comments regarding this burden estimate or any other aspect of this collection of information, including suggestions for reducing the burden to Washington Headquarters Services, Directorate for Information Operations and Reports, 1215 Jefferson Davis Highway, Suite 1204, Arlington, VA 22202-4302, and to the Office of Management and Budget, Paperwork Reduction Project (0704-0188), Washington, DC 20503.

PLEASE DO NOT RETURN YOUR FORM TO THE ABOVE ADDRESS.

1. REPORT DATE (DD-MM-YYYY)

19 April 2000

2. REPORT DATE

3. DATES COVERED (FROM - TO)

30 April 96 - 31 Dec 99

4. TITLE AND SUBTITLE

Numerical, Theoretical and Experimental Studies
A Seafloor and Subseafloor Renovation

5a. CONTRACT NUMBER

5b. GRANT NUMBER

N 00014-96-1-1004

5c. PROGRAM ELEMENT NUMBER

6. AUTHOR(S)

Alistair Harding
Michael Hedlin
John Orath

5d. PROJECT NUMBER

5e. TASK NUMBER

5f. WORK UNIT NUMBER

7. PERFORMING ORGANIZATION NAME(S) AND ADDRESS(ES)

Scripps Institution of Oceanography
9500 Gilman Dr.
La Jolla, CA 92093-0225

8. PERFORMING ORGANIZATION
REPORT NUMBER

UCSD 96-1171

9. SPONSORING/MONITORING AGENCY NAME(S) AND ADDRESS(ES)

Office of Naval Research

10. SPONSOR/MONITOR'S ACRONYM(S)

ONR

11. SPONSORING/MONITORING
AGENCY REPORT NUMBER

12. DISTRIBUTION AVAILABILITY STATEMENT

unrestricted

13. SUPPLEMENTARY NOTES

14. ABSTRACT

See attached report.

15. SUBJECT TERMS

Seafloor renovation, marine acoustics, marine geology

16. SECURITY CLASSIFICATION OF:

a. REPORT

b. ABSTRACT

c. THIS PAGE

17. LIMITATION OF

ABSTRACT

18. NUMBER
OF PAGES

19a. NAME OF RESPONSIBLE PERSON

19b. TELEPHONE NUMBER (include area code)

Final Report for ONR Grant N00014-96-1-1004 "Numerical, Theoretical and Experimental Studies of Seafloor and Subseafloor reverberation" – Alistair J. Harding, Michael A. H. Hedlin, and John. A. Orcutt

This final report is based on the manuscript for our journal article published in the Journal of the Acoustical Society of America as "Migration of backscatter data from the Mid-Atlantic Ridge" – J. Acoust. Soc. Am., 103(4), 1787-1803, 1998.

ABSTRACT

In studies of low-frequency reverberation within the marine environment, a central concern is the relationship between reverberation events and morphological features of the seafloor. A time-domain migration algorithm for the reverberation intensity field is developed that produces scattering coefficient maps coregistered with a bathymetry database. The algorithm is tailored to broadband transient sources with good range resolution, and was developed to analyze an extensive set of reverberation records from a 200-255 Hz source collected on the flanks of the Mid-Atlantic ridge. The precise, sample-by-sample, tracking of wavefronts across elements of the bathymetry database that forms the foundation of the algorithm's implementation results in reverberation maps that show a clear and detailed correlation between scattering and morphology with narrow scarp slopes consistently highlighted. Environmentally induced asymmetries in transmission loss and incidence angle are exploited to break the inherent left-right ambiguity of the receiver array. Iterative migration, assuming a dominant dependence of backscatter on grazing angle, produces images, even from individual records, that show good ambiguity resolution. Results from multiple records corroborate the effectiveness of the ambiguity resolution and demonstrate the stability of the scattering coefficient estimates and the acoustic system.

20000501 133

INTRODUCTION

In July of 1993, a coordinated set of low frequency acoustics experiments were conducted on the western flank of the Mid-Atlantic Ridge within a corridor that lay just north of the Kane fracture zone. These experiments were designed to investigate and quantify the relationship between acoustic reverberation and seafloor morphology and constituted the Main Acoustics Experiment (MAE) of a Special Research Program (SRP)¹ on bottom reverberation sponsored by the Office of Naval Research. Included within the experimental suite were monostatic and bistatic reverberation measurements by the research vessels *Cory Chouest* and *Alliance*, and near bottom measurements of low grazing angle interactions using vertical arrays of hydrophones. One element of the reverberation experiments that makes them unique is the availability of detailed bathymetric and geophysical data for the area, collected on a pair of SRP sponsored large-scale and small scale geophysics cruises. The bathymetric database includes a map of the entire SRP experimental corridor gridded at 200 m and finer scale surveys of selected areas with resolution on the order of 10 m or better. It is the availability of these databases that permits the investigation, in detail, of the correspondence between reverberation returns and bathymetry.

The process of mapping reverberation returns back onto the seafloor scattering sites that produced them can be referred to as charting²⁻⁴. Here we prefer to use the term migration, because of the strong similarity of the methods employed here to the Kirchhoff migration method used in seismic reflection processing. The principal difference between the two is that the reverberation data – beamformed, time-series of acoustic intensity – are assumed to be the result of incoherent scattering rather than coherent reflections. Also, as is the case for seismic migration, we restrict attention to selected primary paths and ignore multiple reflections in the formulation of the method.

In outline, migration is accomplished in two stages; first the seafloor is mapped into the time-beam coordinates of the data, then the reverberation signal from a given beam and small time interval is distributed over the corresponding ensonified area of the seafloor. Migration is complicated by the fact that data were recorded by a horizontal line array (HLA) and each beam is associated with a pair of directions that are oriented symmetrically with respect to the array axis, thus a reverberation return could originate from one of a pair of distinct ensonified areas. Simple mapping schemes that ignore variations in seafloor depth produce reverberation maps that are perfectly symmetric with respect to the array axis and provide no means of resolving, from a single observation, the inherent "left-right ambiguity" introduced by a HLA. Accounting for the bathymetry introduces "environmental symmetry breaking"^{3,4} - bathymetry induced variations in transmission loss, acoustic shadowing - which can be exploited by algorithms, such as the one presented here, to

reduce substantially the left-right ambiguity, even for a single ping. The difference between the environmental symmetry breaking technique and the migration technique presented here is that the former assigns all energy to either the left or right side if the difference in transmission loss reaches a predefined threshold, while the current technique partitions energy according to a set of weights that vary continuously as a function of transmission loss and other factors such as expected backscatter strength.

An additional problem with simpler schemes is that the migrated images are in the time-beam coordinates of individual transmissions rather than in global coordinates of the bathymetry, complicating the comparison of multiple pings and studies of the relationship between scattering and bathymetry. The current migration algorithm avoids this problem by being formulated directly in terms of the backscatter strength of individual elements of the bathymetry grid.

The algorithm is based on a time-domain formulation of the incoherent scattering process which relates the scattering strength to the expected acoustic intensity via a large sparse matrix. This formulation means that we could treat the migration as a linear inverse problem and invert multiple pings simultaneously for scattering strength. Combining pings with diverse look angles would eliminate left-right ambiguity from the solutions. A linear inverse approach would also allow regularization constraints to be employed on the solutions, an approach we pursue elsewhere⁵.

In this paper, we solve the scattering equations approximately using a version of iterative backprojection under the assumption that backscatter strength is spatially isotropic and a function only of the local ensonification and backscatter angles, angles which are equal for the monostatic, direct paths considered here. The advantage of using iterative backprojection is that it is computationally fast and guaranteed to produce migrated images that satisfy the data exactly while only weakly enforcing assumptions about the behavior of scattering strength. Iterative backprojection could potentially be used as a basis for producing well resolved, migrated images in near real time. We use it here to rapidly check the consistency of multiple images from successive reverberation records of the MAE and to produce preliminary estimates of backscattering strength as a function of grazing angle. The linear inverse approach outlined above will only be effective if the individual reverberation images are basically consistent. Uncorrected errors in, for example, array heading or source location would substantially degrade the result of inverting multiple pings.

We concentrate on the analysis of a subset of the data, namely half convergence zone ($1/2$ CZ), monostatic reverberations from broadband, 200-255 Hz, linearly frequency modulated (LFM) transmissions recorded by the *R/V Cory Chouest*. We chose this subset because it has the best range resolution and simplest propagation paths, and thus affords the best opportunity of investigating,

quantitatively, the relationship between backscattering strength and bathymetry. Previous examinations of the SRP acoustics data have, for the most part, concentrated on the longer range, continuous wave (cw) data, and have established that there is a broad correspondence between high amplitude reverberations and well ensonified features at 1/2 and 1 1/2 CZ, with the highest returns from backfacing ridges. However, the detailed investigation and quantification of this relationship is as yet incomplete; this paper represents one step in that process.

I. OVERVIEW OF DATA AND EQUIPMENT

The MAE was conducted within an approximately 4° by 2° corridor on the flanks of the Mid-Atlantic ridge extending from 45° W to 49° W and from 25° 30' N to 27° 30' N. The corridor lies within a larger area designated as an ONR natural laboratory⁶, which straddles the Mid-Atlantic ridge itself and is bounded to the south by the Kane fracture zone. The seafloor fabric within the corridor is dominated by lightly sedimented, ridge parallel abyssal hills, but there are also large sedimented ponds and the area is dissected by deep corridors that are the fossilized, off-axis expression of spreading segment boundaries at the ridge axis. The feature whose backscatter we will examine in detail here is a ~30 km long abyssal hill, designated B', that lies at the western end of one of the segment boundary corridors. In particular we will concentrate on a set of 1/2 CZ, monostatic reverberation returns recorded by the *R/V Cory Chouest* that span the intersection of a pair of the experimental runs, run 5a and run 6, Fig. 1 and Table I. This intersection lies slightly northwest of a large set of intersecting tracks that constitutes the focus of an extensive set of bistatic and monostatic experiments that had B' as the primary target. We have chosen the first intersection here because the associated transmissions provide better ensonification of the front slope of B' at 1/2 CZ.

The basic features of the *R/V Cory Chouest* source and receiver arrays are shown in Fig. 2. The vertical source array consisted of 10 elements spaced at 2.29 m and centered at 101 m, while the horizontal receiving array consisted of 128 hydrophone groups spaced at 2.5 m. Beamforming of the reverberation data was performed aboard ship using a delay and sum beamformer with a Hamming window, resulting in a nominal broadside beamwidth of ~1.3°, measured at the -3 dB point. The presence of dead or improperly gained phones in the HLA resulted in nearly uniform sidelobe level of approximately -30 dB¹.

The schedule of source transmissions for the experiment was conceptually arranged in a hierarchical fashion with the bottom two levels in the hierarchy being transmission segments and individual source wavetrains or pings. Segments were numbered consecutively and each one lasted 12 minutes. Ping numbers were also numbered consecutively with typically 6 source wavetrains being

transmitted during each segment. For the portions of runs 5a and 6 examined here, 2 out of every 3 segments were used for *R/V Cory Chouest* transmissions and the remaining segment for *Alliance* transmissions. One of the standard, usually the first, transmissions within a *Cory Chouest* segment was a 5 s. duration linearly frequency modulated (LFM) signal chirped over the band 200-255 Hz. It had the largest bandwidth of any of the source wavetrains and hence the best range resolution after matched filtering, $\Delta r = 13.6$ m; it is thus the best choice for examining, in detail, the spatial structure of the scattering process.

The structure of the LFM source wavefield out to beyond a $1/2$ CZ is shown in Fig. 3. The broadband transmission loss was calculated by integrating across the band, the transmission losses predicted at individual frequencies by a wide-angle parabolic equation (PE) code⁷. At times during the experiment the source array was steered down at various angles with respect to the surface, but for the transmissions of interest and the calculation, the steering angle was set at 0° . The sound speed profile, displayed in Fig. 3a, was essentially the same throughout the experiment and the sea state was calm. The center of the source array at 181 m was in the upper part of the waveguide with the conjugate depth being at 3800 m and the turning range, $1/2$ CZ distance, being around 33 km. The core of the main acoustic beam contains a pair of high amplitude fringes which result from the interference between energy that was up and downgoing at the source level. Behind the core, the two components are sufficiently separated in time, up to ~ 30 ms, that there is no significant interference effect on the amplitude. Furthermore in this region the ray propagation angles diverge by about 2° (Fig. 4). Beyond the turning range, most of the structure in the main beam is due to caustics in either the up or downgoing source field. The source field also has a number of sidelobes that intersect the seafloor at ranges less than 15 km.

II. MIGRATION ALGORITHM

The goal of the migration algorithm is to produce a map of scattering strength registered on the same grid as the bathymetry data. The basic observational data are the intensity time series $I(\varphi_b, t)$ associated with beam angle φ_b that result from squaring the matched filtered and beamformed pressure series. For direct, reciprocal paths between source/receiver and the scattering site, the relationship between the expected intensity of the backscattered signal and the scattering coefficient is taken as the following integral over the seafloor

$$I(\varphi_b, t) = \iint dA \gamma m(x, \theta, \phi) g(x, \varphi_b, \varphi_a, t - T_r - T_s) \quad (1)$$

where

$$\gamma = \gamma_{mf} \gamma_r \Psi_r \gamma_s \Psi_s p_T^2 T \quad (2)$$

$T_{r,s}$ are the ray theoretical travel times to and from the scattering location. γ is the product of the transmission losses, $\Psi_{s,r}$, to and from the seafloor; the gains, γ_s , γ_r , and γ_{mf} , associated with the source array, receiver array and matched filtering; and the source level, a product of the transmission level, p_T , and signal duration, T . Since we are dealing with broadband transient signals, gains for individual components of the system are defined in terms of the ratio of integrals over the input and output pressure fields⁸ –

$$\gamma = \int_0^{T_o} dt p_o^2(t) / \int_0^{T_i} dt p_i^2(t) \quad (3)$$

The scattering coefficient, $m(x, \theta, \phi)$ in Eq. (1), is a function of position, x , and the monostatic incidence/backscatter direction at the seafloor (θ, ϕ) . The quantity $g(x, \phi_b, \phi_a, t - T_r - T_s)$ can be termed the scattering function for the system, it depends on the details of the scattering process, as well as quadratically on the effective source function at the seafloor and quadratically on the time domain response of the beamformer for a given steering angle ϕ_b and arrival angle ϕ_a at the receiver array. The partition of scattering between the scattering coefficient and the scattering function is defined by normalizing $g(t)$ so that its time integral is unity.

For direct paths, Eq. (1) is a time domain variant of the standard equation relating the expected reverberation intensity to scattering coefficients for cw signals^{8,9}. The additional element in the time domain formulation is the introduction of g , which can be regarded as representing the resolution function of the acoustic imaging system. Analytic expressions or empirical forms could be found for g (and also m), given explicit assumptions about the nature of the surface, for example small amplitude roughness⁸. In practice, we assume that the details of the time response will not be important provided that the resulting scattering coefficients estimates represent averages over a sufficiently large area. We thus use a simple factored boxcar form for g

$$g(\phi_b, \phi_a, t) = g^*(t) b(\phi_b, \phi_a) = B(t/t_w) B((\phi_b - \phi_a)/\Delta\phi) \quad (4)$$

where $B(t)$ is a unit boxcar centered at zero and width one, and $b(\phi_b, \phi_a)$ is the beamformer response, which is in turn simplified to a boxcar of width $\Delta\phi$, the angular separation between adjacent beams. In the limit $t_w = 0$, the time dependence, $g^*(t)$, reduces to a δ -function. A potentially more accurate representation of the angular dependence would be to use the response function of the beamformer at a representative frequency rather than a boxcar.

We can derive a sonar equation from Eq. (1) by substituting for the scattering function from Eq.

(4). With $g^*(t)$ set equal to a δ -function, integrating from t_1 to t_1+T_a yields

$$\bar{p}_R^2 T_a = \Psi_r \Psi_s \cdot \gamma_{mf} \gamma_s \gamma_r \cdot p_T^2 T \cdot m \cdot A \quad (5)$$

where

$$\bar{p}_R^2 = \frac{1}{T_a} \int_{t_1}^{t_1+T_a} I(\varphi_b, t) \quad (6)$$

and A is the ensonified area corresponding to the integration limits in time and beam angle, and it is assumed that transmission losses etc. are constant over A . This is equivalent to the following sonar equation for the reverberation level $R = 20 \log p_R$

$$R = -TL_r - TL_s + G + M + 10 \log(A) + S - 10 \log(T_a / T) \quad (7)$$

where $TL_{r,s}$ are the transmission losses, G is the combined system gains, M the scattering strength and S the source strength, all defined in the obvious way from Eq. (5). The final term corrects for differences between the averaging time and the signal duration. Frequently for cw signals the averaging time is chosen equal to the pulse duration and there is no correction. However, for the LFM pulse, choosing an averaging time equal to the width of the matched filtered pulse, 18 ms, corresponds to a correction of 24 dB. A problem with choosing a short averaging time is that it is then hard to justify the use of a δ -function for the scattering function, since effectively the convolutional nature of the reverberation process is being ignored.

The above result is most naturally viewed as producing a scattering strength map in the local time-angle coordinates of the beamformer: the scattering strength estimate obtained from Eq. (7) is assigned to the area A bounded by a pair of isochrons and a pair of beam boundaries. We wish, instead, to produce a scattering strength map in terms of a global coordinate system and thus we will use Eq. (1) to reexpress the reverberation intensity in terms of contributions from individual bathymetry elements. To this end, we again use the factored form of the scattering function, Eq. (4), and assume that all quantities, except g^* , associated with a small patch, k , of the bathymetric grid are constant. The scattering response of patch k can then be approximated as

$$I_k(t) = \gamma_k m_k g^*(t)^* \frac{dA_k}{dt} = \gamma_k m_k G_k(t) \quad (8)$$

where, for notational convenience, we have incorporated the beamformer factor $b(\varphi_b, \varphi_a)$ into the general gain factor γ_k . dA_k/dt is the rate at which the patch area is swept out by the isochrons; it is

zero for $t < T_{\min,k}$ and $t > T_{\max,k}$, the minimum and maximum travel times associated with the patch. Convolution of g^* with the sweep rate function acts to smooth g^* , suggesting, once again, that the knowledge of the details of the scattering is not critical provided that estimates are averages over large enough areas, a necessary condition for which is that $T_{\max,k} - T_{\min,k} \gg t_w$.

The total scattered intensity of a single beam is the sum of the individual patches responses, i.e.

$$I(t) = \sum_k I_k(t) = \sum_k \gamma_k m_k G_k(t) \quad (9)$$

The summation implicitly includes the left-right ambiguity of the receiving array through the patch weighting γ_k , since the beamformer factor is nonzero only along the conjugate beam directions. As before Eq. (9) could be explicitly averaged by integration over a time intervals T_a which would serve to stabilize the individual intensity values and reduce the size of the subsequent matrix equations. If the scattering function is taken as a δ -function, averaging yields

$$\bar{p}_R^2(t)T_a = \sum_k \gamma_k m_k A_k f_k(t) \quad (10)$$

where A_k is the area of the k th patch and f_k is the fraction of the area of the k th patch ensonified during the averaging interval. If the fractional contributions are rounded to 0 or 1, then Eq. (10) is equivalent to Eq. (5) of Ref. (2). In the latter, a synthetic test case was considered with the source wavetrain taken as 2s long cw pulse and the averaging time taken equal to the pulse length, resulting in multiple seafloor patches contributing to a single averaged intensity measurement. In practical applications, though, it would be difficult to justify the use of a δ -function when the duration of the source pulse is long relative to the size of the individual patches, since implicitly, as noted above, it ignores the convolutional nature of the reverberation process. A scattering function whose duration matched that of the cw pulse would be more appropriate, but even so the structure of the function would potentially be important for good scattering estimates.

A direct discretization of Eq. (9) for time samples at $t = j\Delta t$ is

$$I_j = \sum_k I_{jk} = \sum_k G_{jk} \gamma_k m_k \quad (11)$$

Individual beam responses from multiple pings can be combined to form a single, large matrix equation relating reverberation to the scattering coefficients of the patches. For the datasets considered below, the number of scattering coefficients would be ~30,000, and the number of intensity samples ~20,000, a value which increases proportionately if multiple pings are combined. However, the matrix is sparse since $K(j)$, the number of patches illuminated at time sample, j , is on the

of order 10 for a single ping.

The matrix equation could be solved as a least squares problem with the addition of regularization constraints on the scattering coefficients, using any suitable sparse matrix solver such as conjugate gradients¹⁰ or LSQR¹¹, an approach we investigate elsewhere⁵. Here we choose to solve the inverse problem approximately using a form of iterative backprojection. The advantage of backprojection is that it is simple, fast and robust, while at the same time capable of providing a fair degree of ambiguity resolution; we use it here to check the ping-to-ping consistency of the reverberation data. Although, backprojection does not have the potential resolution of more complete inversion methods, especially for multiple pings, these methods will not perform optimally unless the data are essentially consistent and we can be assured that there are no unresolved problems with ship position and array orientation⁴.

For a single beam, the intensity contribution assigned to a patch k at time sample j by the backprojection is proportional to the weighting factor for that patch

$$I_{jk} = w_k I_j \quad (12)$$

where

$$w_k = \frac{\gamma_k \cdot G_{jk}}{\sum_{k \in K(j)} \gamma_k \cdot G_{jk}} \quad (13)$$

The backprojection thus incorporates a degree of ambiguity resolution, assigning intensity based on such factors as transmission loss to the ensonified patches and also on the basis of the area swept out - a face pointing more directly into the acoustic beam will attract proportionately higher assigned intensity.

The result of the backprojection is an estimate of the scattering intensity function $I_k(t)$ associated with each patch k . An estimate of the scattering coefficient, m_k , is found by integrating the scattering intensity, Eq. (9), and using the fact that the integral of $g^*(t)$ is unity and thus the integral of $G(t)$ is A_k , the area of patch k . The discrete time version of the estimate is

$$m_k = \frac{\sum_j I_{jk}}{\gamma_k A_k} \quad (14)$$

or substituting for γ_k

$$m_k = \frac{1}{A_k} \frac{(\gamma_{mf} \gamma_r \Psi_r)^{-1} \sum_j I_{jk}}{\gamma_s \Psi_s p_T^2 T} \quad (15)$$

This latter form shows explicitly that the scattering coefficient estimate is, as it should be, the ratio of the scattered intensity to the incident intensity, scaled by the area.

The summation over the individual intensity contributions helps to stabilize the scattering coefficient estimate for each patch. A rough estimate of its expected variance can be obtained by considering the variance of the contributing intensity values, assuming the w_k are approximately constant. The time bandwidth product for the LFM pulse and 200 m patches is approximately 15, thus the expected variance of the sum is approximately 1 dB^{12,4}.

If a patch is illuminated by more than one beam, then the scattering coefficient estimate is modified appropriately to become a weighted sum of the individual beam contributions,

$$m_k = \frac{1}{A_k} \frac{\sum_n \sum_j I_{jkn}}{\sum_n \mu_{kn} \gamma_{kn}} \quad (16)$$

where μ_{kn} is the fractional area of patch k illuminated by beam n and γ_{kn} is the appropriate gain factor for the beam.

In the examples examined later, we have employed an iterative form of the backprojection in which the weighting function in Eq. (12) is modified to

$$w_k = \frac{\gamma_k \cdot \hat{m}_k \cdot G_{k,j}}{\sum_{k \in K(j)} \gamma_k \cdot \hat{m}_k \cdot G_{k,j}} \quad (17)$$

where \hat{m}_k is the scattering coefficient estimate from the previous iteration. The numerator is now the predicted scattering intensity for each patch, and the effect of the backprojection, when there is a mismatch between the predicted and recorded intensities, is to modify each of the assigned intensities by an equal decibel increment.

The backprojection method has similarities to the "environmental symmetry breaking" approach of Ref. 3, particularly on the first iteration when the factor controlling the assignment of energy is usually transmission loss. The difference between the two is that Ref. 3 requires the difference in transmission loss to reach a threshold before assigning all energy to one side, while here assign-

ment of energy changes continuously as a function of the weighting factors.

The above formulation is essentially a local one, relating a deterministic reverberation signal, consisting of sections of elevated intensity, to scattering produced by direct paths to and from the seafloor. Local volume scattering can be considered to be included as part of the scattering signal via the scattering function g . All other contributions to the recorded reverberations, including non-local, multiple scattering and long-range, sub-seafloor refraction paths are grouped together as noise. Forward modeling using a PE approach indicates that multipath contributions to the reverberation field are not significant for ranges below a $1/2$ CZ except as diffuse arrivals that fill in the noise floor. However, compact multipath arrivals do become significant in the time interval immediately beyond the direct path $1/2$ CZ returns, where they fill what other would be an acoustic shadow zone (13A). In principle, it would be possible to incorporate multiple scattering in the above formulation by including suitable ray paths. However, such an approach would quickly become unwieldy if many paths were included, and would itself require an a-priori parameterization of the scattering process, which is one of the objectives of the study. Full wave solutions, such as PE, automatically handle the multipath problem but do not circumvent the need for prior parameterization. The validity of the local scattering assumption and the possible influence of multipaths can be examined, a-posteriori, by determining whether there are any regions of high scattering coefficient not associated with identifiable bathymetric features or that are not stable between migration images.

III. IMPLEMENTATION DETAILS

In implementing the migration algorithm for the SRP data, we used as the grid for the scattering coefficient map the 200 m by 200 m swath bathymetry grid from the Hydrosweep survey. This grid size is smaller than the nominal cross track resolution of the beamformed data, which is ~ 600 m at broadside at $1/2$ CZ, but expressed as an ensonification duration, 270-380 ms, it is considerably greater than the 18 ms duration of the compressed LFM pulse. For such a broadband signal, the compressed pulse width yields an optimistic estimate of range resolution, since the actual resolution would depend strongly on the duration of the scattering response, including the surface reflection delay at the source/receiver. Whether the 200 m grid is large with respect to the scattering function duration can be checked a-posteriori by assessing the stability of the scattering strength maps.

The quantities needed for backprojection of a given ping are calculated in two stages, first relevant propagation quantities such as travel time and ray angles are found at the vertices of the

grid, then the sweep function $G(t)$, is estimated for each 200 by 200 m grid element, which we refer to here as a patch. The spatial homogeneity of the sound speed profile during the MAE, ignoring small scale fluctuations, permits a considerable reduction in computational effort: propagation quantities are not found directly by three-dimensional ray tracing but are instead interpolated from fields calculated on regular two-dimensional, range-depth, grids. This simplification to a one-dimensional profile also makes it computationally feasible to use PE calculations, rather than less accurate ray theory, to estimate broadband transmission losses. Two sets of PE results were calculated, one with a ten element source array for the forward direction, the other with a single element at the HLA depth for the reverse direction, assuming reciprocity. The single frequency results were then integrated across the source band to obtain the broadband TL estimates (c.f. Figure 3). The effects of the free surface reflection are included in the amplitude terms of the migration via the TL calculation. However, only one set of travel times for the downgoing ray paths are calculated, thus the theoretical resolution is degraded by at least the time difference in the up and downgoing ray paths, ~20 ms (c.f. Figure 4).

The properties of the individual patches are calculated from the vertex values. The patches are assumed planar, and their orientation is found by a least squares fit to the vertex depths. Similarly the isochron surfaces of two-way travel time are assumed to be locally planar and are found by a least squares fit to the travel times at the vertices. In the following examples, we take the scattering function, $g(t)$ to be a δ function, and thus the sweep function, $G(t)$ for a patch is comprised of a series of straight line segments with vertices corresponding to times when the wavefront passes a patch vertex (Fig. 5). From Fig. 5, it is evident that using a more complex short duration function rather than a δ -function, for example a 18 ms boxcar, would have only a minor effect on the scattering coefficient estimates after averaging.

Geometric shadowing calculations were performed prior to migration using a mean bathymetric profile along each beam direction. A small transition region of 300 m was added to the edge of each ensonified region in order to help prevent small numerical artifacts or local roughness from producing shadow zones. Thus individual patches that point away from the local ray direction were considered ensonified, and it was left to the migration to determine whether they produced small backscatter. During backprojection, the scattering strengths of patches in the shadow zones were adjusted at each iteration in order to produce an expected backscattered intensity equal to the 10th percentile of the ensonified patches. The purpose of this was to ensure that the preponderance of energy would be assigned to an ensonified area if the conjugate side was in shadow, while at the same time permitting energy assignment if both sides were in shadow. In this way it was possible

to keep track of unexpected scattering sites in the reverberation map.

The migration algorithm was implemented primarily in MATLAB but with the sweep functions for individual patches calculated by an external C function. The first stage of the algorithm, the calculation of propagation quantities at the vertices of the grid took 6 minutes of CPU, and the second stage took 7 minutes per iteration on a HP 715/75 workstation (SPECint95 3.1, SPECfp95 3.6). MATLAB is an interpreted environment and we conservatively estimate that these times could be reduced by a factor of four if the algorithm was implemented as compiled code.

IV. MIGRATION EXAMPLE FROM B'

We take as an initial migration example, ping 1313 of segment 415, for which the *R/V Cory Chowest* was located just north and west of the center of the track star near ridge B', Fig. 1, and had a HLA heading of 169° , Table I. At a 1/2 CZ on the starboard side is B' with its backfacing scarps oriented almost perpendicular to the beam directions, while at the same range on the port side, a series of N25°E trending ridges point almost directly into the beam directions (Fig. 1). The reverberation returns from these ridges and the scarp of B' interfere to produce a set of crossing, high amplitude events in the data between 30 and 45 s, Fig. 6. When we examine the two-way transmission loss to the conjugate areas, we find that only the port side ridges and the upper part of B' are shallow enough to project into the center of the acoustics beam, although a broad platform on the port side is also well ensonified, Fig. 7.

Fig. 8 displays the reverberation map obtained after the first iteration of the migration using data from 20s out to times corresponding to the 1/2 CZ turning ranges. The reverberation map is an intermediate backprojection output and is calculated from the sum of the backscattered energy associated with each patch of the grid, Eq. (12). The reverberation map is a stable estimate in the sense that backprojection is guaranteed to be intensity preserving, and the partition of energy between simultaneously ensonified patches is affected only by relative not absolute errors in, for example, transmission loss. From Fig. 8 we can see that the high amplitude backscatter events are predominantly located within areas that were strongly ensonified. However, a notable exception is the strong scattering associated with a line of small scarps on B' in the region (2955-2970, 205-210) UTM km, which lies well outside the main acoustic beam. Furthermore, it is reassuring that within the strongly ensonified regions the reverberation events tend to be localized along bathymetric features with high slopes, such as the scarps covering the upper parts of B'. This impression is supported by Fig. 9, which shows that above a cutoff of about 10° the

mean scattering strength increases with local grazing angle, a dependence that arises even though the a-priori assumption is that the scattering coefficient is constant. The cutoff angle of about 10° represents the point at which the scattering strength curve reaches the noise floor, approximately 30 dB below the maximum scattering strength. The primary source of noise is cross-talk between the beamformed channels and thus the usable dynamic range of the ARSRP reverberation data is set by the -30 dB side-lobe level of the beamformer. The influence of the cross-talk noise on the ARSRP reverberation data is nicely demonstrated by finite-difference modeling studies¹³.

Although, the initial migration produces a fair degree of left-right ambiguity resolution, it is clearly not perfect if local slope is the sole or primary determinant of backscatter strength. For example, energy that on the starboard side is associated with the scarps of B', also appears on the port side where it cuts across the mostly shallow slope bathymetric fabric. We can test the degree to which slope accounts for strong backscatter by incorporating the estimated angular dependence of the scattering coefficient into the partition coefficients for the backprojection, Eq. (17). All events associated with high slope features will migrate solely to the appropriate left or right image, only anomalous events will remain ambiguous and appear on both images. For this dataset, the migration effectively converged after three iterations, with only a barely perceptible change in the mean backscatter coefficient between iterations 3 and 4, Fig. 9. The perceived ambiguity in the backscattered energy images is significantly reduced and only a few small isolated events appear split between the two images, Fig. 10. The effectiveness of the ambiguity resolution is more readily assessed in the original time-beam coordinates, Fig. 6. For the most part this view confirms the impression that the energy is cleanly split between the left and right side. However, energy near the edges of some prominent reverberation events leaks through to the other side, suggesting that there may be a slight error in the array orientation or that the migrated image could be improved by incorporating some cross talk between beams in the beamformer factor b , Eq. (4).

The scattering strength map for the 4th iteration is displayed in Fig. 11. As expected the elongated scarp slopes on B' are highlighted in the image, but compared to the energy image, the prominence of the port ridges is reduced, their previous prominence being due solely to strong ensonification. As was to be expected from the mean behavior, there is an overall correspondence between the grazing angle and scattering strength with the normalization emphasizing the scattering strength of the lower slopes. Also, predictably, the scattering strength map is noisier than the reverberation one, since now global as well as local errors in estimated quantities are important. For example, any mismatch between the predicted and actual pattern of transmission loss will be reflected in the scattering strength map.

V. COMPOSITE IMAGES OF B'

We can assess the validity of the single ping ambiguity resolution and simultaneously gain insight into the general quality of the data by comparing the migration results from multiple ensonifications of the same target with nearly the same ship location but different headings. The standard means of obtaining multiple looks at a target is to use reverberation records from crossing paths and this we do by comparing images from runs 5a and 6 of the MAE which cross at an angle of approximately 25° . But we can also gain useful information from multiple pings from a single run, taking advantage of small changes in the heading of the receiver array between pings. If a reverberation event is migrated to its true origin on the seafloor, then its location will not change when the array heading changes by θ . Conversely a false scatterer that resulted from migrating energy to the wrong side of the array will rotate through 2θ since it is located at the mirror image of true scatterer in the array, Fig. 12. Thus the incorrectly migrated energy will move in a predictable fashion in step with the changes in array orientation. This movement can most readily be appreciated by combining the migration results from successive pings into an animation sequence. For the 5 consecutive LFM pings from run 5a considered here, the maximum difference in array heading is 3° which is sufficient to move false scatterers across 3-4 beams in the migrated image.

We have investigated the consistency of the migrated images using 5 consecutive broadband LFM pings from both run 5a and run 6 spanning their intersection at $26^\circ 36' \text{ N}$, $-47^\circ 47' \text{ W}$ ((2946, 222), Fig. 1.). Fig. 13 displays the scattering strength maps for the northern foreslopes of B' for 9 of the pings. Perhaps the most striking aspect of the images is that relatively narrow scarp slopes appear consistently, with only relatively minor ping-to-ping variation in strength and location. The images from run 6 (pings 1683-1696) are cleaner than the ones from run 5a (pings 1313-1336) due to the fact that the conjugate area on run 6 is the source of much less backscatter. For run 5a, the lower portion of the images below 2950 includes residual mislocated energy from the port side ridges. A port side origin is supported by the fact that it does not appear in the images from run 6 and that its location moves between the successive run 5a images. Similarly energy that appears in the run 5a images near the center of a small basin at (2960,202) can also be attributed to a partial failing of the ambiguity resolution.

Averaging the individual images effectively suppresses false scatterers attributable to energy leakage and multipaths and emphasizes the consistency of direct path, high backscatter from the narrow ridges, Fig. 14. All the high backscatter regions correspond to scarp features that are ensonified at high local grazing angles. However, the converse is not true, there are features, most notably the front edge of a small platform centered (2955, 198) that although illuminated at high angle does not

produce high backscatter. Spots of high backscatter do appear along the front edge of the platform in the individual migration images, perhaps indicative of backscatter speckle that fluctuates in response to changes in the ensonification. However, since the strongest backscatter events appear in the noisier run 5a images it is more likely that the high ensonification angles succeed in capturing port side energy during migration.

For each of the 10 pings, we have used the migration results to estimate the variation of mean backscatter strength with grazing angle, Fig. 15. The backscatter curve was found using the Loess algorithm¹⁴, assuming that the local grazing angles were correct. The Loess algorithm finds a point on the backscatter curve for a given grazing angle by fitting a line to a subset of the data centered on the grazing angle using weighted least squares. Formal confidence intervals for the mean were estimated from 200 bootstrap samples¹⁵ for each ping, and were typically 1-2 dB at the 95 % confidence level, increasing at high grazing angles. Over the interval from 10° to 45°, the mean scattering strength curves for run 5a are roughly comparable to a Lambert's law type behavior with a Mackenzie parameter of -27 dB, although the curves are distinct based on the formal confidence intervals. The backscatter estimates for a given grazing angle are distributed approximately normally with a standard deviation of 4-5 dB, Fig. 16.

The split is probably a consequence of differences in the distribution of the relatively small number of patches that are ensonified at high grazing angles. For run 5a, 73% of the 700-900 patches ensonified at angles greater than 25° (approximately 3% of the total) come from the B' scarps, while for run 6, this percentage drops to 63% with a greater number of high angle targets on the starboard side that are small and relatively isolated. When the backscatter curves are split into port and starboard contributions, the gap between the starboard side curves that includes B' is reduced, although not eliminated. Moreover, the port side targets display a weaker dependence on angle, Fig. 17, and are consistent over the two runs. The difference in scattering strength may indeed reflect an intrinsic difference in the backscatter level between the areas. However, it may also be a consequence of processing artifacts and of the limitations of the bathymetry database. The size of the port side targets tend to be near or below the angular resolution of the system, and thus the intrinsic averaging of the beamforming coupled with any small errors in the heading calculations will tend to mute the influence of high angle patches. Also the number of high angle targets is small enough that imperfections in the bathymetry database such as small noise spikes that produce erroneous high angle targets would bias the scattering strength estimates downward.

VI. CONCLUSIONS

We have developed an algorithm for migrating reverberation data that is based upon time-domain expressions for the expected intensity of the reverberation field. The time dependent aspects of the field are parameterized by a function referred to as the scattering function, which includes both stochastic components dependent on the details of the seafloor scattering and deterministic ones due to the characteristics of the acoustic imaging system. We argue that the details of the scattering function are not critical provided that scattering coefficients are estimated over patches of the seafloor with response times that are long compared with the characteristic time of the scattering function, or equivalently whose area is large compared to the correlation scales of the scattering process⁹. This approach is comparable to reducing speckle in optics by averaging over a scanning aperture¹⁶. Time averaging has the additional advantage of producing stable estimates from individual reverberation records, the trade-off is that spatial resolution is reduced. However, even with averaging, the broadband LFM pulse of the SRP experiments is capable of yielding consistent scattering strength estimates at the resolution of the main bathymetry database.

A key feature of the algorithm is that the results are computed in the global coordinate system of the bathymetry database rather than the beam-travel time coordinates of individual pings, facilitating the comparison of results from multiple pings. The basis for the coordinate conversion is the precise, sample-by-sample, tracking of the acoustic wavefronts across the individual patches and the assumption that the scattering coefficient is constant within individual elements, patches, of the bathymetry database. These two assumptions allow us to reexpress the reverberation response as a large sparse matrix equation with the scattering coefficients as the unknowns. The matrix formulation enables multiple records to be combined simply into a single linear inversion problem.

In this paper we have taken a processing oriented approach taking advantage of the sparsity to solve the matrix equation approximately using iterative backprojection rather than attempting to solve the equation directly as part of a linear inversion. We describe this process as migration since the method is analogous to the Kirchoff migration procedure of seismic processing, the principal difference being that here it is applied to incoherent scattering rather than coherent reflections. It has the processing virtue of producing reverberation and scattering coefficient maps rapidly thus facilitating efficient analysis of multiple records. The reverberation maps, which are produced by backprojection as an intermediate output, represent an exact partition of the record intensity and are thus guaranteed to be stable and allow us to assess directly the effectiveness of the left-right ambiguity resolution.

The performance of the migration algorithm is illustrated using two sets of broadband monostatic

reverberation records from a pair of crossing runs of the SRP experiment on the flanks of the Mid-Atlantic ridge. At a 1/2 CZ, iterative migration produces well resolved maps of reverberation and scattering strength. In the reverberation maps, there is a clear correspondence between the location of high amplitude reverberation events and bathymetric features with either low transmission loss, high local grazing angle or both. In particular, narrow scarps less than 1 km wide are highlighted consistently. The migration also produces a plausible resolution of the left-right ambiguity, dividing the majority of events in a reverberation record cleanly between the two ensonified areas. The migration algorithm can be regarded as an environmental symmetry breaking method that uses seafloor induced asymmetries to resolve the inherent left-right ambiguity of the receiving array. Although the migration images are by no means unique, the improvement of the event separation with iteration and the clear correspondence between events and bathymetric features provides strong a-posteriori justification for the inclusion of mean backscatter strength as a factor in the backprojection weights.

The results of multiple migrations from a single run and from crossing runs corroborates the overall effectiveness of the left-right ambiguity resolution for individual records, and supports the idea that scattering strength is primarily a function of grazing angle. The majority of high scattering strengths areas, primarily associated with scarp slopes, appear consistently in all migration images. A few potentially anomalous areas move in step with changes in array heading within a single run and tend to be absent in images from the crossing run. These areas are identified as energy misassigned to the wrong side of the array, and are attenuated when multiple maps are stacked together. Employing multiple heading directions from crossing runs is the standard means of reducing left-right ambiguity. The present results demonstrate that even small heading changes (e.g 2-3°) from a single run can be profitably employed to reduce ambiguity. The consistency of the migration images demonstrates the stability of the acoustic imaging system used for the SRP experiments and is a good indication that linear inversion could be applied successfully to the data.

The migration results indicate that transmission loss and grazing angle are the dominant factors controlling reverberation response in the study area. A dependence, in the mean, of backscatter strength on grazing angle appears after the first iteration of the migration when the backprojection weights contain no bias towards patches with high grazing angles. We thus conclude, as have previous investigators^{3,8,17}, that the correlation, in the mean, between backscatter strength and grazing angle is a robust feature of the data.

Weaker dependencies of scattering strength on spatial and azimuthal variations in scattering strength were not explicitly sought for in the present analysis. However, the difference in the mean

scattering curves between B' and the conjugate sides, Fig. 17, indicate that there may be an azimuthal dependence resolvable in the data. The prominent ridges of B' are ensonified almost perpendicular to the structural grain, whereas the starboard side ridges with the weaker backscatter are ensonified parallel to the grain. Resolution of questions such as azimuthal dependence of backscattering or the influence of sediments on backscattering will require further, more detailed analysis of the data.

Above a noise floor of about 5° , the estimated dependence of the mean scattering strength on grazing angles is approximately equal to, but formally statistically distinct from, that of Lambert's law with a Mackenzie parameter of -27 dB. Although the general magnitude of the increase in backscatter strength appears robust, the detailed dependence on grazing angle must be treated with some caution as the accuracy of the slopes derived from the swath bathymetry is itself questionable, especially when the high slopes are associated with smaller features near the resolution limit of the system¹⁸.

REFERENCES

- ¹Acoustic Reverberation Special Research Program, Initial Report, edited by J. A. Orcutt (Scripps Institution of Oceanography, 1993).
- ²N. C. Makris, Imaging Ocean-basin Reverberation via Inversion, J. Acoust. Soc. Am., **94**, 983-993, (1993).
- ³N. C. Makris, and J. M. Berkson, Long-range Backscatter from the Mid-Atlantic Ridge, J. Acoust. Soc. Am., **95**, 1865-1881, (1994).
- ⁴N. C. Makris, L. Z. Avelino, and R. Menis, Deterministic Reverberation from Ocean Ridges, J. Acoust. Soc. Am., **97**, 3547-3574, (1995).
- ⁵M. A. H. Hedlin, A. J. Harding, and J. A. Orcutt, manuscript in preparation.
- ⁶B. E. Tucholke, K. C. Macdonald, and P. J. Fox, ONR Seafloor Natural Laboratories on Slow- and Fast-spreading Mid-Ocean Ridges, EOS, Trans. AGU, **72**, 268-270, (1991).
- ⁷M. D. Collins, A Split-step Pade Solution for the Parabolic Equation Method, J. Acoust. Soc. Am. **93**, 1736-1742, (1993).
- ⁸C. S. Clay and H. Medwin, *Acoustical Oceanography : Principles and Applications*, (Wiley, New York, 1977).
- ⁹L. M. Brekhovskikh and Y. P. Lysanov, *Fundamentals of Ocean Acoustics*, (Springer Verlag, New York, 1991), 2nd ed.
- ¹⁰G. H. Golub & C. F. Van Loan, *Matrix Computations*, (Johns Hopkins University Press, Baltimore, 1989), 2nd ed.
- ¹¹C. C. Paige, and M. A. Saunders, LSQR: An Algorithm for Sparse Linear Equations and Sparse Least Squares, ACM Trans. Math. Softw., **8**, 43-72, 1982.
- ¹²I. Dyer, Statistics of Sound Propagation in the Ocean, J. Acoust. Soc. Am., **48**, 337-345, (1970).
- ¹³J. O. A. Robertsson, A. Levander, and K. Holliger, Modeling of the Acoustic Reverberation Special Research Program deep ocean seafloor scattering experiments using a hybrid wave propagation simulation technique. J. Geophys. Res., **101**, 3085-3101, (1996).
- ¹⁴W. S. Cleveland, Robust Locally Weighted Regression and Smoothing Scatter Plots, J. Am. Statist. Ass., **74**, 829-836, (1979).
- ¹⁵B. Efron, and R. J. Tibshirani, *An Introduction to the Bootstrap*, (Chapman & Hall, New York, 1993).
- ¹⁶B. R. Frieden, *Probability, Statistical Optics, and Data Testing : A problem Solving Approach* (Springer-Verlag, New York, 1991), 2nd ed.

¹⁷K. B. Smith, W. S. Hodgkiss, and F. D. Tappert, Propagation and analysis issues in the prediction of long-range reverberation. *J. Acoust. Soc.* 99, 1387-404., 1996.

¹⁸M. C. Kleinrock, Capabilities of Some Systems used to Survey the Deep Sea floor, in *CRC Handbook of Geophysical Exploration at Sea*, edited by R. A. Geyer (CRC Press, Boca-Rotan, 1992), 2nd ed.

Run	Segment	Ping	Location (Deg)		Location (UTM km)		HLA Array
			Lat	Lon	Lat	Lon.	Heading
5a	415	1313	26° 38.6' N	-47° 48.6' W	2950.1	220.3	168.6
5a	417	1318	26° 37.4' N	-47° 48.1' W	2947.8	221.1	166.1
5a	420	1327	26° 35.7' N	-47° 47.5' W	2944.7	221.9	169.5
5a	421	1331	26° 35.2' N	-47° 47.3' W	2943.7	222.3	169.1
5a	423	1336	26° 34.0' N	-47° 46.9' W	2941.4	222.9	167.6
6	547	1683	26° 38.7' N	-47° 47.3' W	2950.2	222.5	197.3
6	548	1687	26° 38.1' N	-47° 47.4' W	2949.1	222.2	195.9
6	550	1692	26° 36.9' N	-47° 47.6' W	2946.9	221.8	194.8
6	551	1696	26° 36.3' N	-47° 47.7' W	2945.7	221.6	194.6
6	554	1705	26° 34.5' N	-47° 48.1' W	2942.4	220.9	195.3

Table I: List of reverberation records, pings, analyzed in this paper

Figure Captions

FIG. 1. Bathymetry and a portion of *R/V Cory Chouest* track lines (heavy black lines) in the vicinity of target B', an elongated ridge at the western edge of the Fig. In this paper we analyze reverberation data from Pings at the start of run 5a and 6 of the MAE (heavy white circles).

FIG. 2. Sketch of the source and receiver array of the *R/V Cory Chouest*. The 10 element source array had a spacing of 2.29 m while the 126 element receiver array had a spacing of 2.5 m.

FIG. 3. (a) Representative up (blue) and downgoing (red) rays paths within the main acoustics beam from a point source at 181 m, the center depth of the vertical source array. The reference sound speed (black) has a surface velocity of 1540 m/s and a minimum velocity of 1494 m/s at 1.1 km. The downgoing ray paths are simple but caustics form beyond the 1/2 CZ at 30-35 km. (b) PE calculation of the transmission loss for a broadband, 200-255 Hz, source from the 10 element source array. Transmission loss variations near the axis of the downgoing main beam are the result of interference of the downgoing and surface refracted energy. Transmission loss is more variable beyond a 1/2 CZ due to the presence of caustics.

FIG. 4. (a) Grazing angle of rays at a depth of 3.5 km. Arrivals are for rays from the top, middle and bottom elements of the source array. There is approximately a 2° difference in ray angle between surface reflected/refracted rays, upper cluster, and rays leaving the source travelling downwards. At this depth, the penumbra of the main beam starts at 25 km and extends to about 28 km. (b) Difference in travel times at 3.5 km for up and downgoing rays at the source.

FIG. 5. Example sweep area function for a seafloor patch. The sweep function consists of linear segments with joints corresponding to the passage of the beam wavefront (dash lines) past the patch vertices. For the calculation both the patch and wavefront are assumed locally planar. (Patch area is normalized to unit area).

FIG. 6. (a) Reverberation data for ping 1313, broadband LFM transmission of s415. The displayed data spans the time interval of reverberation returns from 1/2 CZ and beam numbers 15-120, which avoids endfire (Beam nos. 64/65 are the broadside beams). To facilitate comparison with the reverberation maps, the data has been averaged over an interval of 270 ms and corrected for the average number of ensonified patches, a correction of -11.1 dB. The prominent returns between 30 & 45s are a combination of returns from scarps on the front face of B' on the starboard side of the array and ridges on the port side that point almost directly into the beams. (b) & (c) estimated port and starboard time series after iterative migration. The split is plausible and for the most part clean, although some residual energy appears to be misplaced.

FIG. 7. Two way transmission loss for ping 1313 projected onto the port and starboard side bathymetry. Strongly ensonified features include the top of B' on the starboard side, and the high ridges pointing approximately into the beams on the port side. The uppermost parts of the two prominent ridges on the port and starboard side colored white project up above the acoustic beam and are thus not included in the calculation. The current figure does not take into account geometric shadowing.

FIG. 8. Reverberation map from the initial migration of ping 1313. The left-right ambiguity resolution is based primarily on ensonification level, although some dependence on local incidence angle is included via the sweep rate function. High amplitude returns due to local slope such as those from the scarp slopes of B' are not fully resolved and also appear in the conjugate image.

FIG. 9. Estimate of backscatter strength as a function of grazing angle for the 4 migration iterations of Ping 1313. Iteration 1- dotted, 2- dash-dot, 3-dashed, 4-solid. For iteration 1 there is no-apriori assumption of increased backscatter with grazing angle, yet the mean backscatter strength shows a correlation with grazing angle down to the noise floor at about 10°. For subsequent iterations the mean backscatter of the previous iteration is used and convergence occurs in 3-4 iterations.

FIG. 10. Reverberation map of ping 1313 after four iterations. Compared to iteration 1, the left-right ambiguity resolution is significantly improved, with a much weaker ghosting of the B' scarps in the port side image.

FIG. 11. Scattering strength maps derived from the reverberation map, Fig 10., by correcting for transmission loss, area, etc. The previous prominence of the top of B' and the port side ridges is revealed as primarily a consequence of high ensonification levels, while the B' scarp slopes are identified clearly as regions of high backscatter.

FIG. 12. With incomplete ambiguity resolution, energy from a scatterer will also be migrated to a false scatterer location; that is, the mirror image in the line array of the true location. These locations will remain paired for different pings (black circles) if the ship heading remains constant, but the location of the false scatterer will rotate through 2θ when the array heading changes by θ .

Fig. 13. Scattering coefficient maps of a subarea of the B' abyssal hill for 5 consecutive broadband LFM pings of run 5a, 1313 through 1336, and 4 consecutive pings for run 6, 1683-1696. Most of the scarp slopes in the area show up consistently as regions of high backscatter. A notable exception is the edge of a small platform near (2955,200) which is only intermittently highlighted possibly only as the result of being mistakenly assigned energy from the conjugate area.

Fig. 14. Comparison of the mean backscatter strength, left panel, found by stacking the 10 migrated pings, with the mean illumination angle, right panel, expressed in terms of the cosine of the local grazing angle. For the most part, there is a close correspondance between high backscatter targets and local grazing angle: all prominent backscatter targets correspond to scarp features ensonified at high grazing angles. However, there are some features, most notably the front slope of a small platform centered (2955, 198) that although illuminated at high angle does not produce a high backscatter.

FIG. 15. Estimate of scattering strength vs. grazing angle for pings from run 5a (solid) and run 6 (dashed) with bootstrap estimates of $\pm 2\sigma$ errors in the mean. For reference, Lamberts law curve using a Mackenzie parameter of -27 dB is included, dotted curve.

FIG. 16. Representative histogram of scattering strength relative to mean trend from ping 1313 for a bin extending from 21° - 29° . There are 1385 patches in the bin. The distribution is approximately gaussian with $\sigma = 4.4$ dB

FIG. 17. Port and starboard estimates of mean scattering strength for the 10 pings. Estimates from run 5a are solid lines and those from run 6 are dashed. The estimates from the starboard side that ensonify B' show a consistently stronger dependence on grazing angle and there is less of a gap between run 5a & 6 estimates.

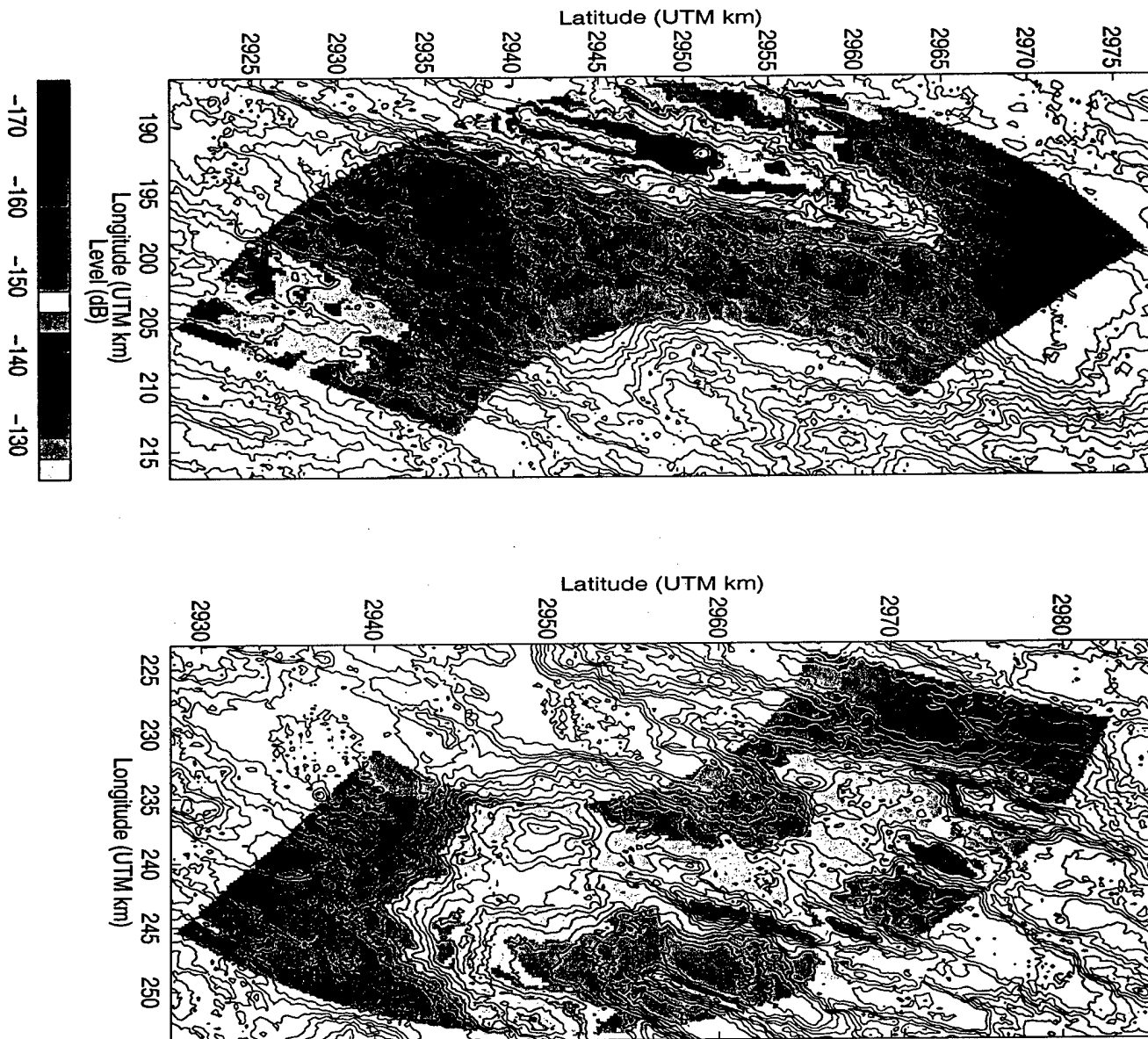


Figure 1

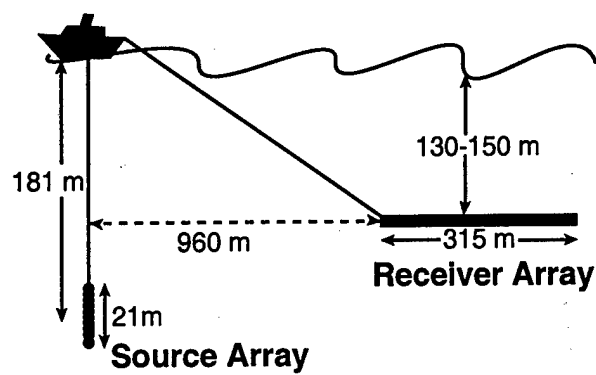
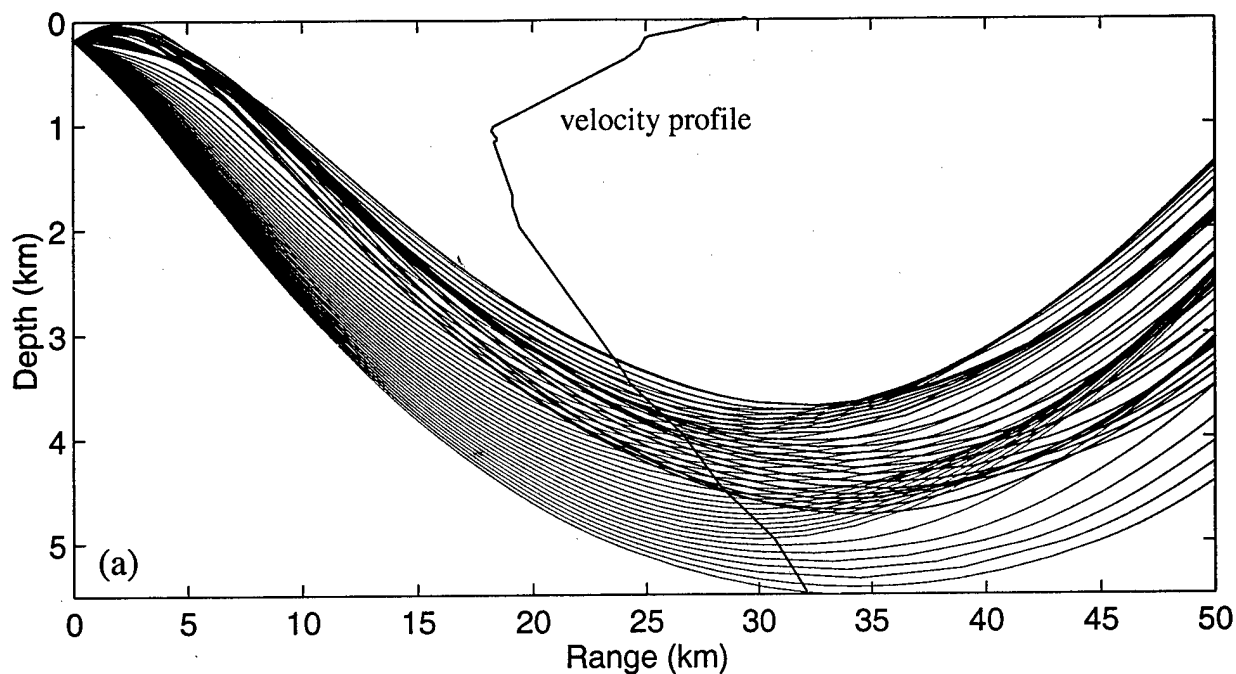


Figure 2



Transmission loss for SRP source array 200–255 Hz

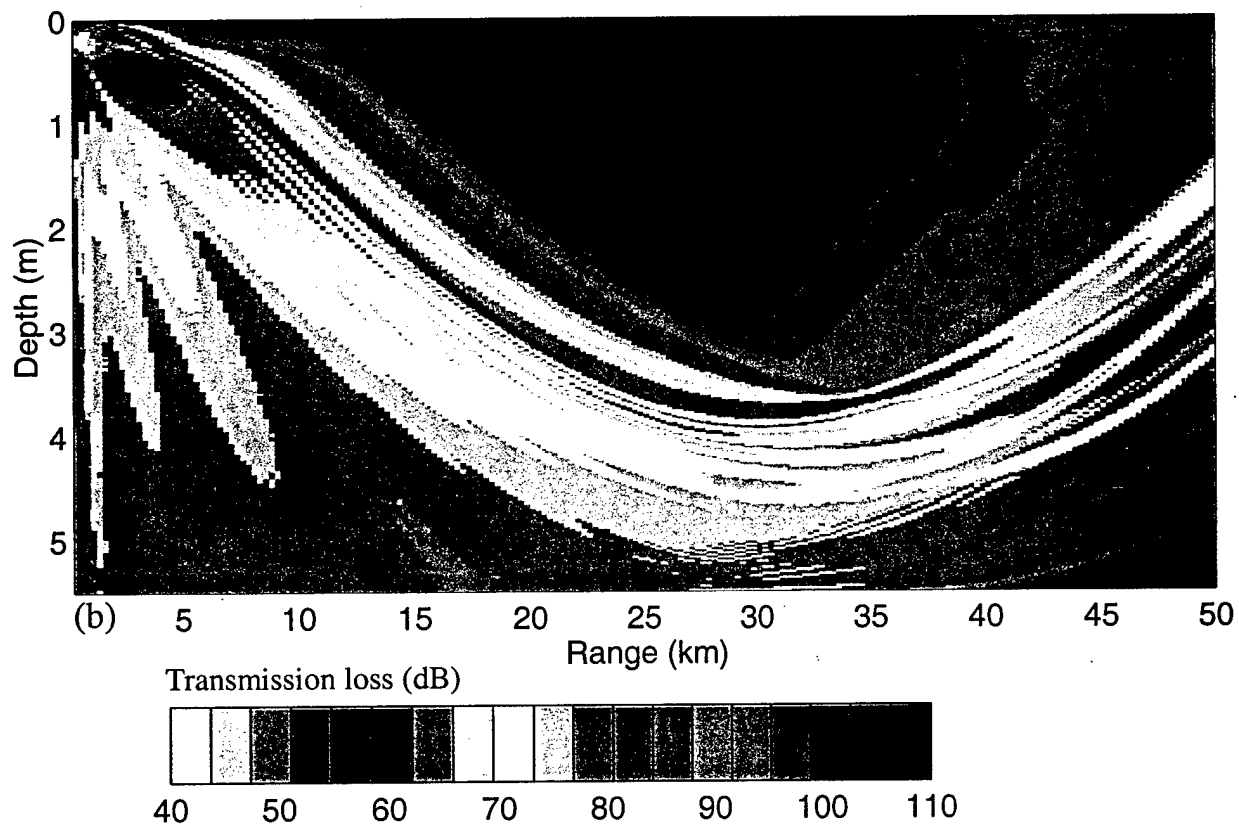


Figure 3

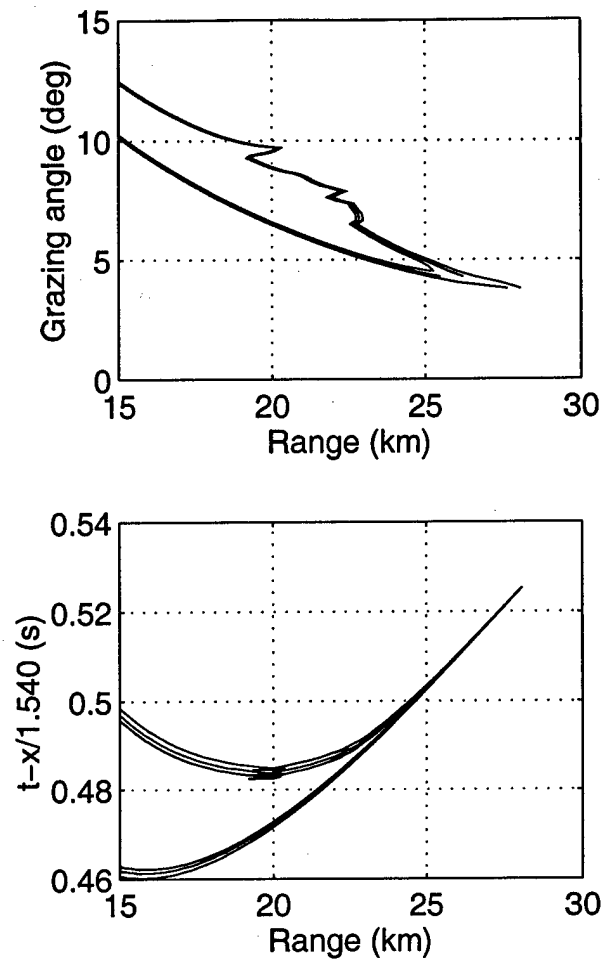


Figure 4

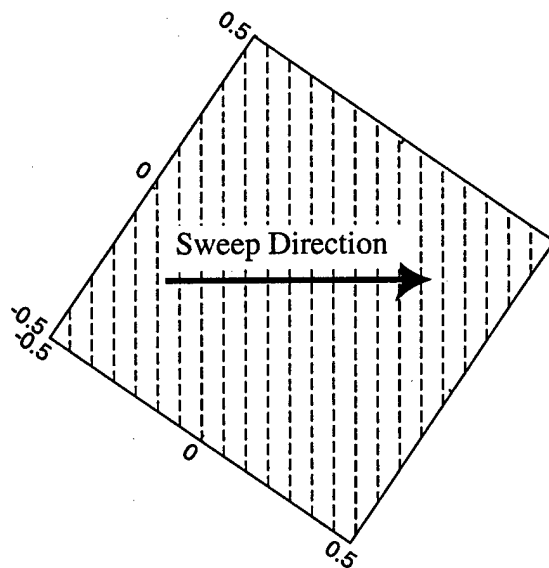
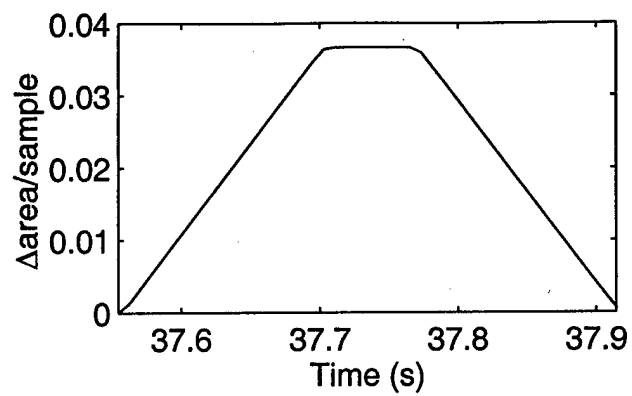


Figure 5

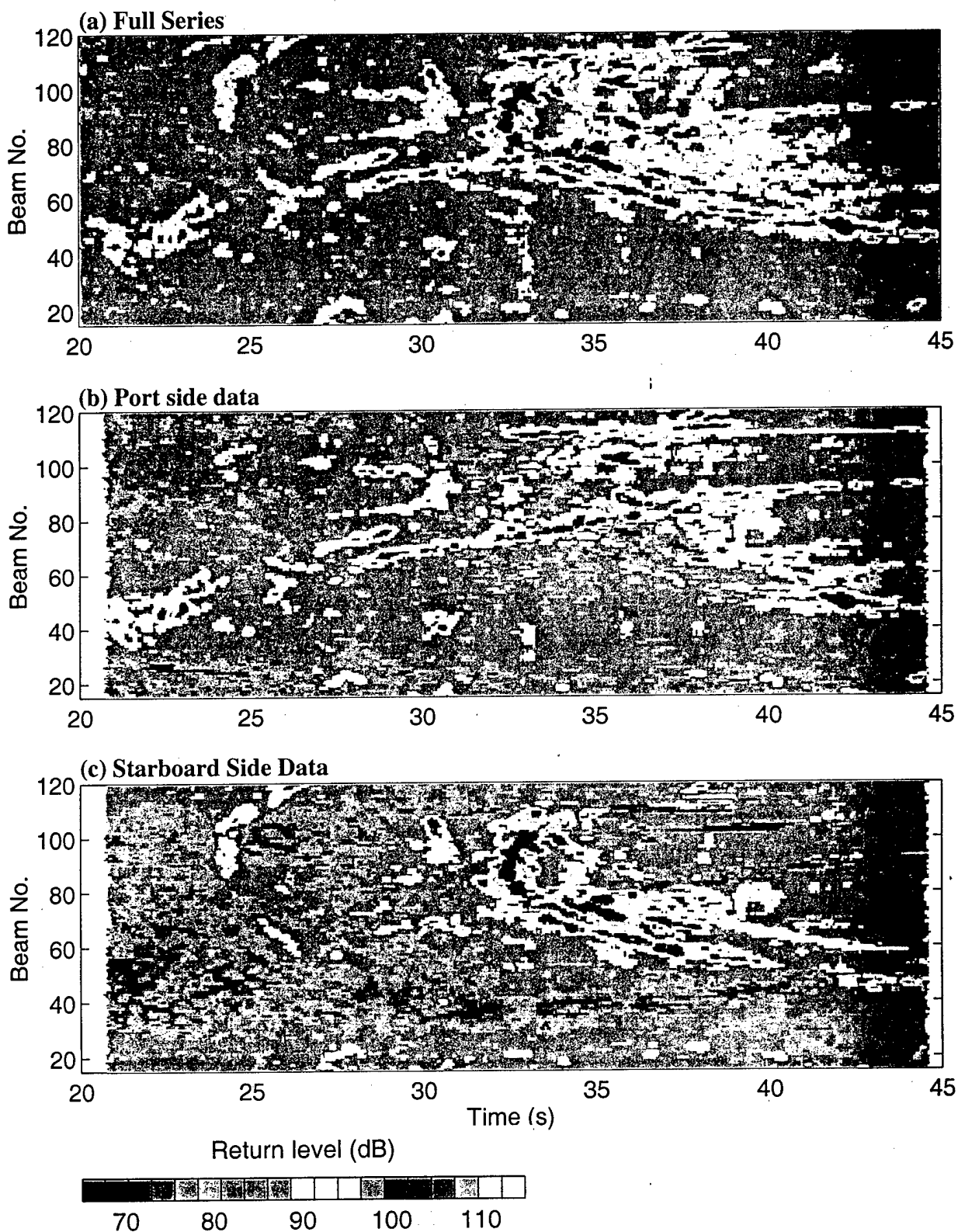


Figure 6

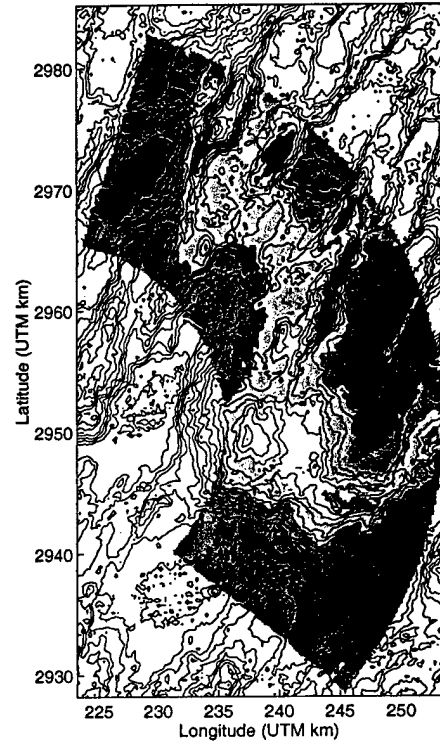
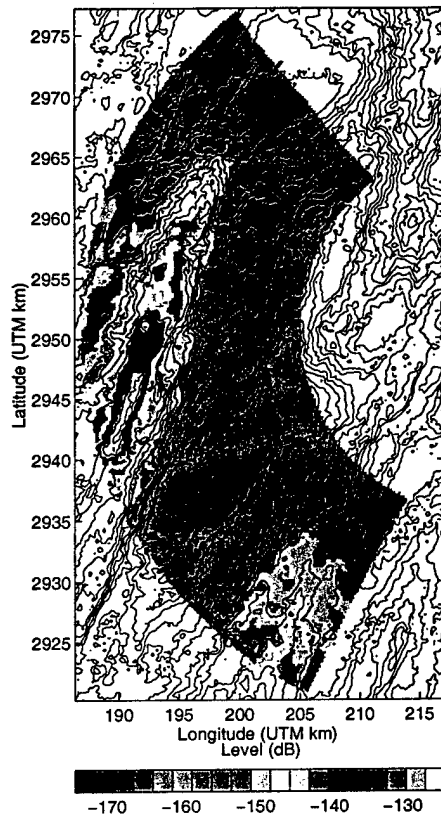


Figure 7

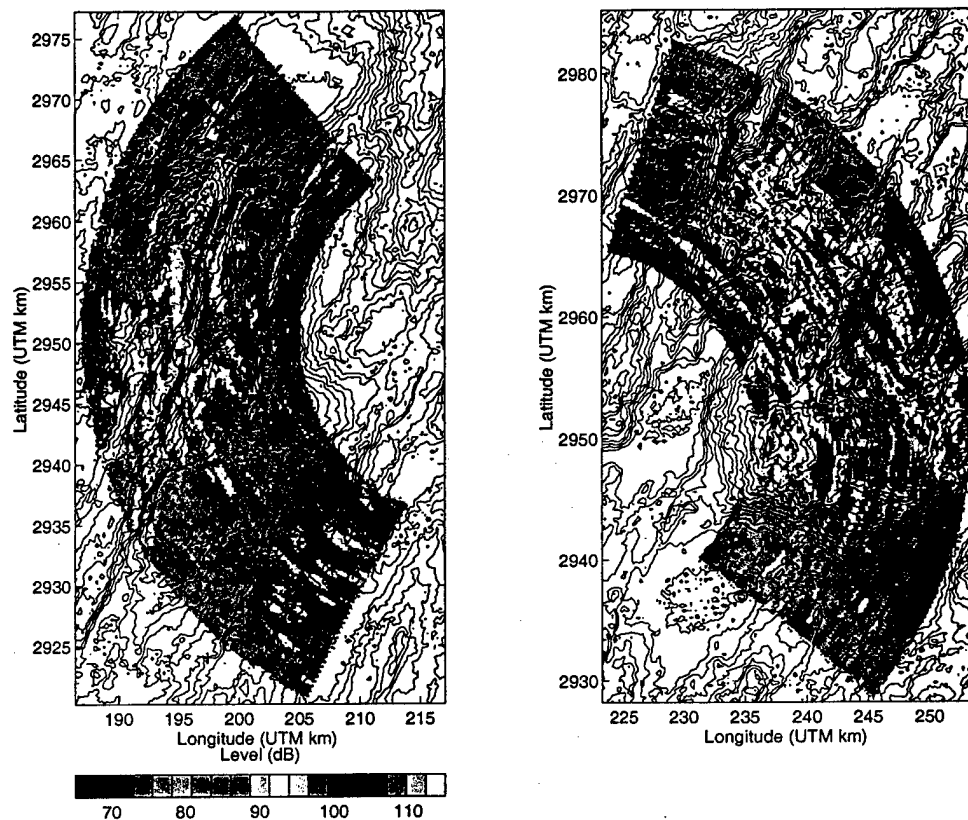


Figure 8

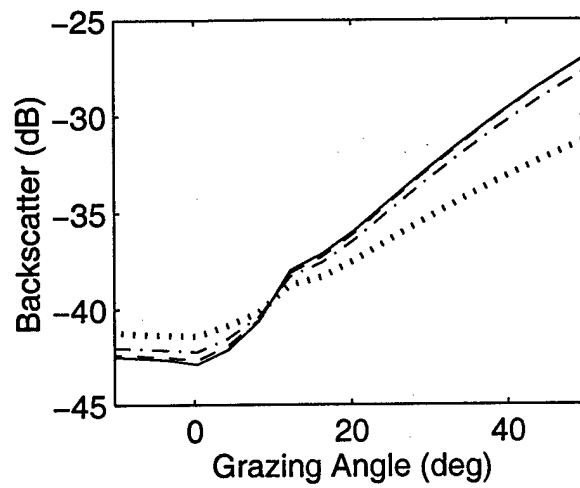


Figure 9

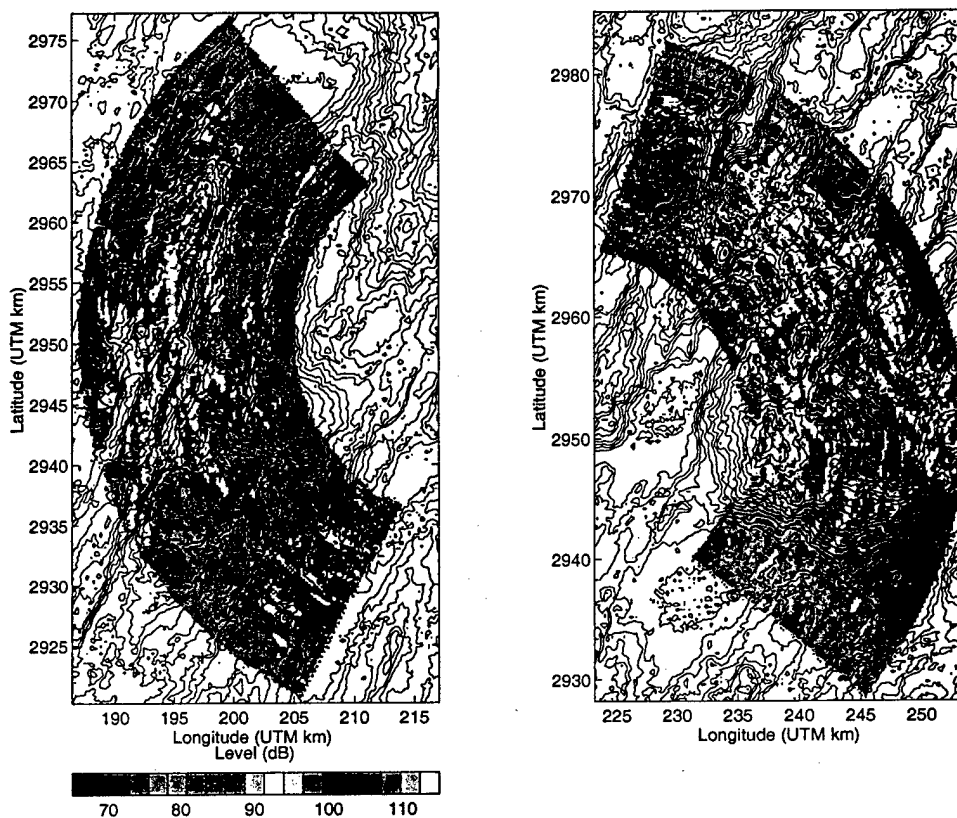


Figure 10

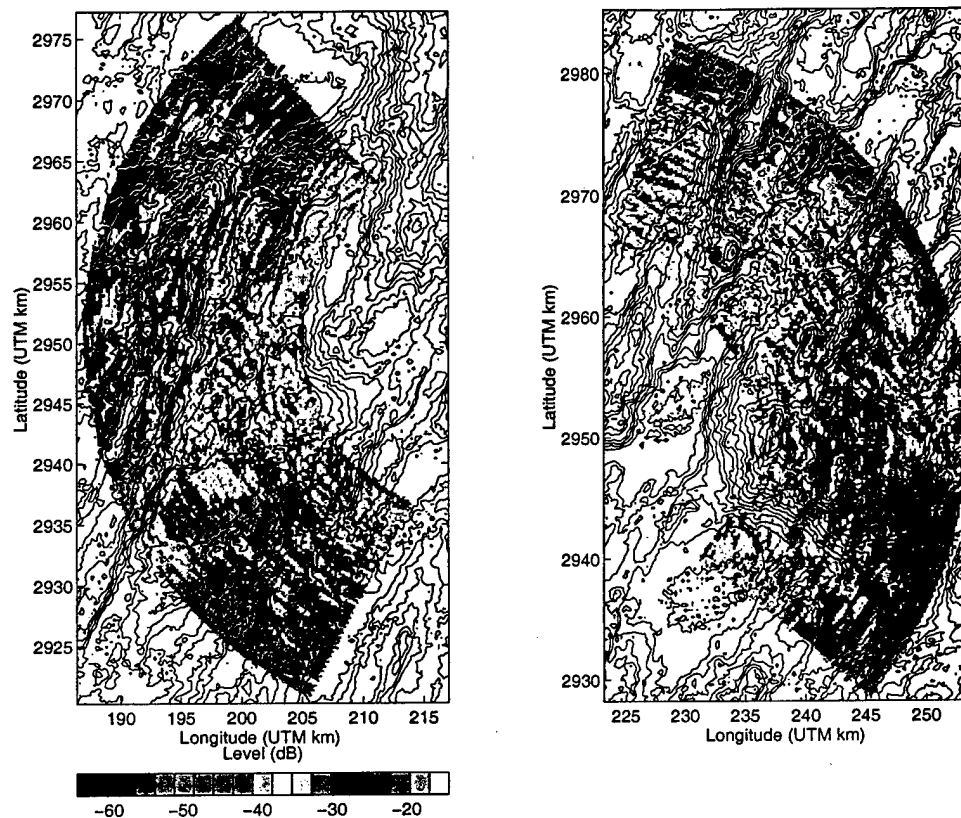


Figure 11

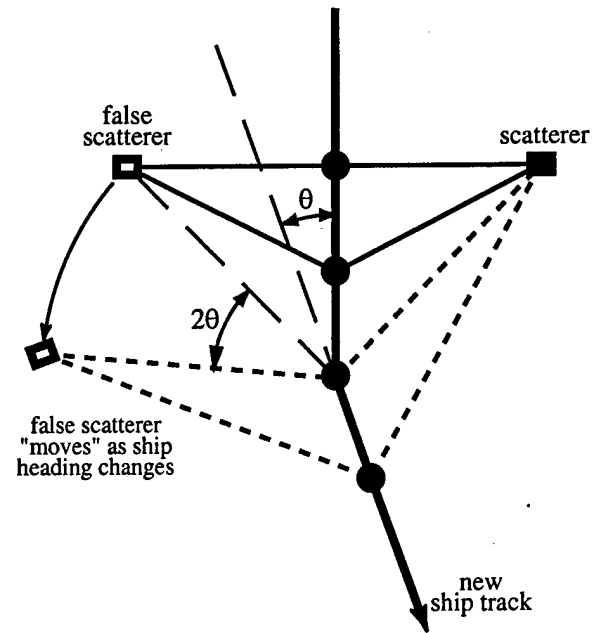


Figure 12

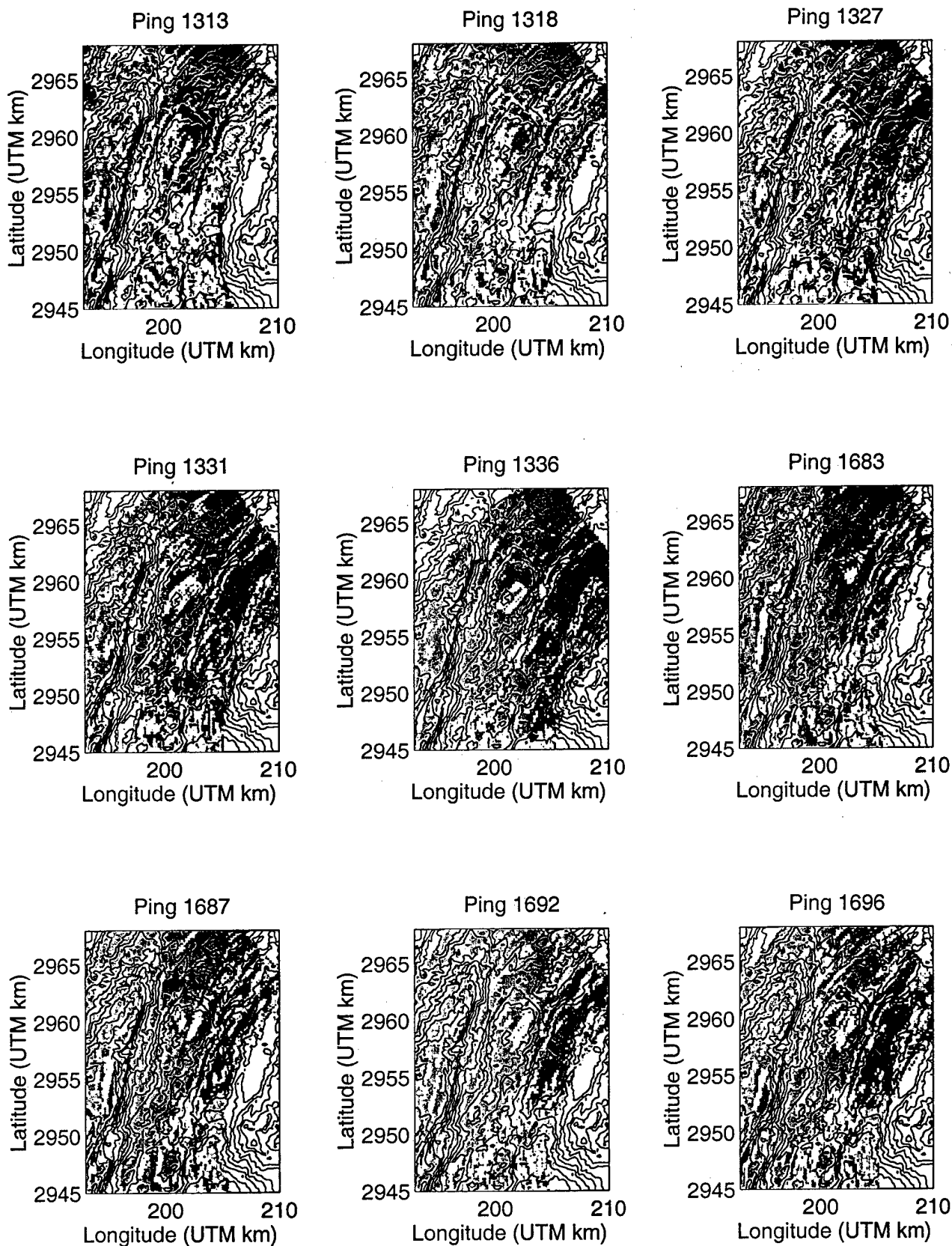


Figure 13

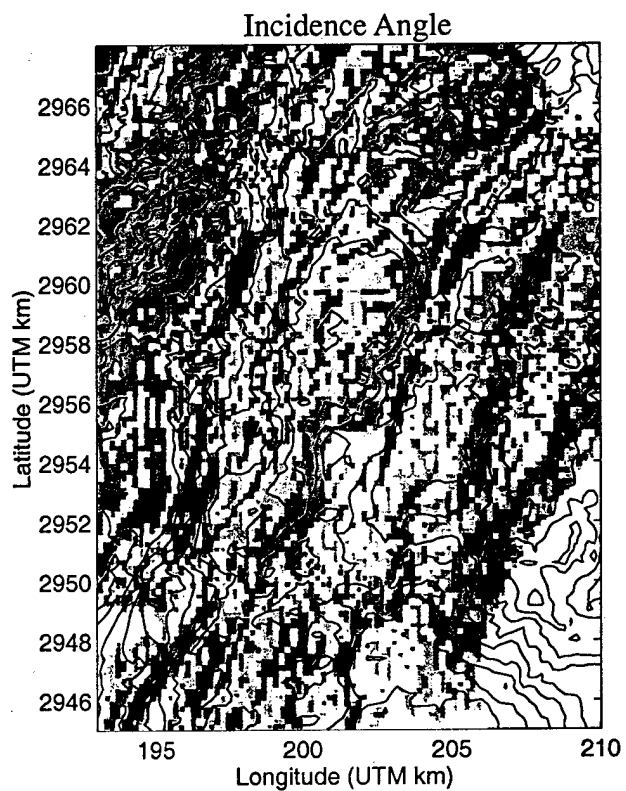
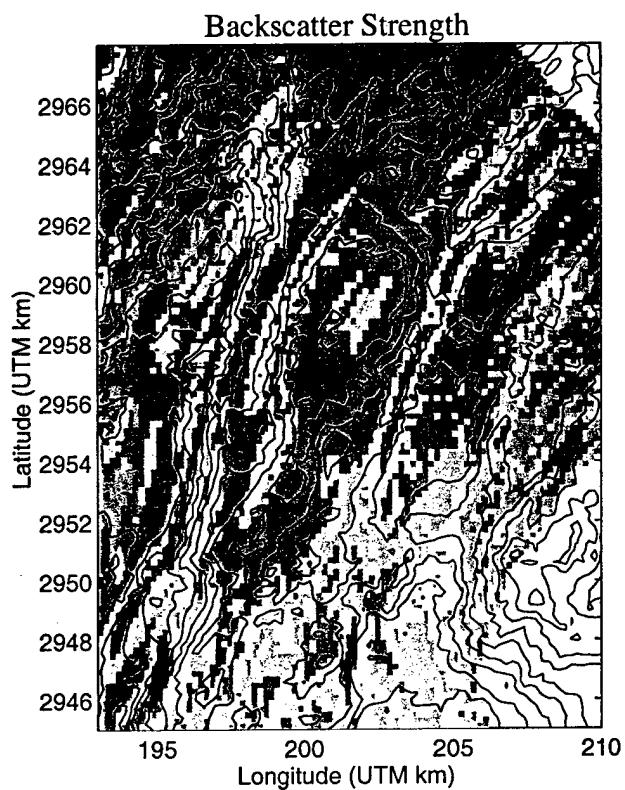


Figure 14

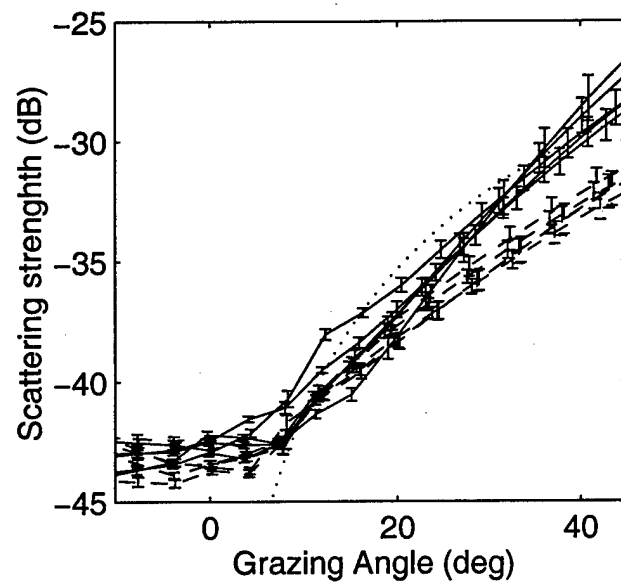


Figure 15

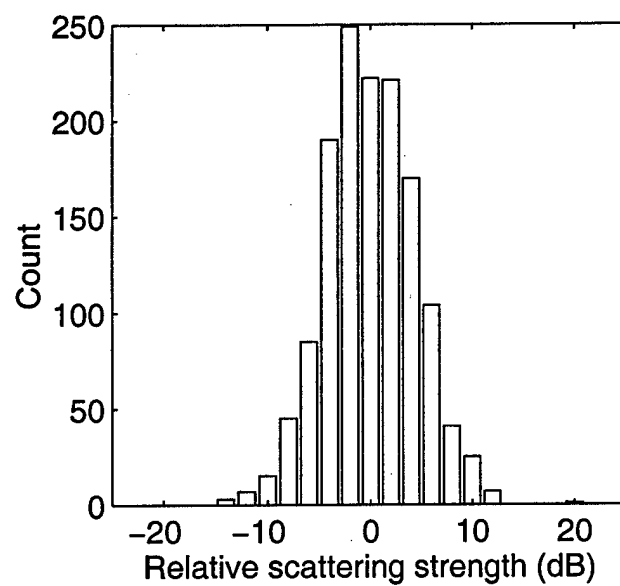


Figure 16

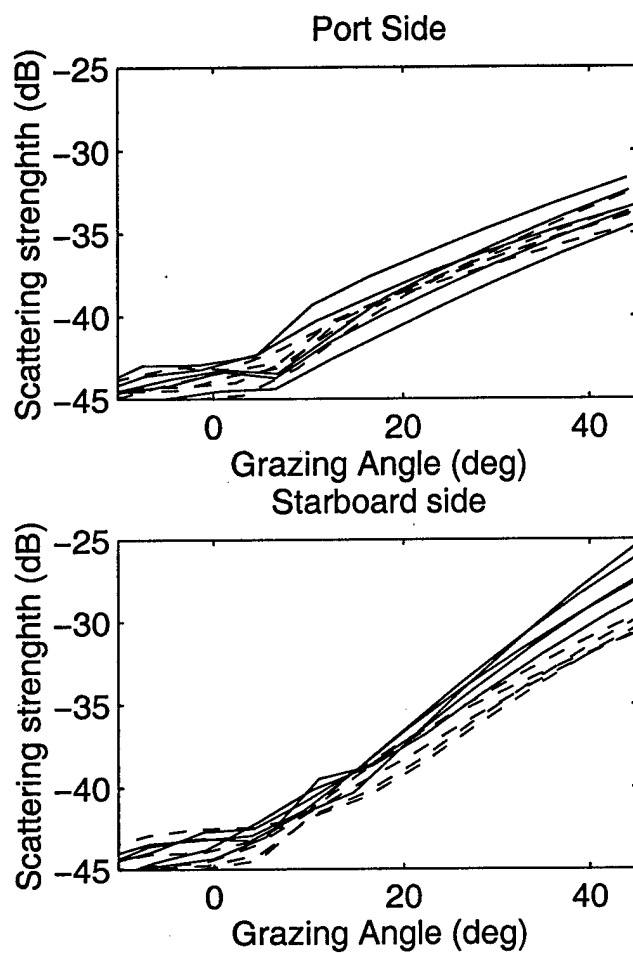
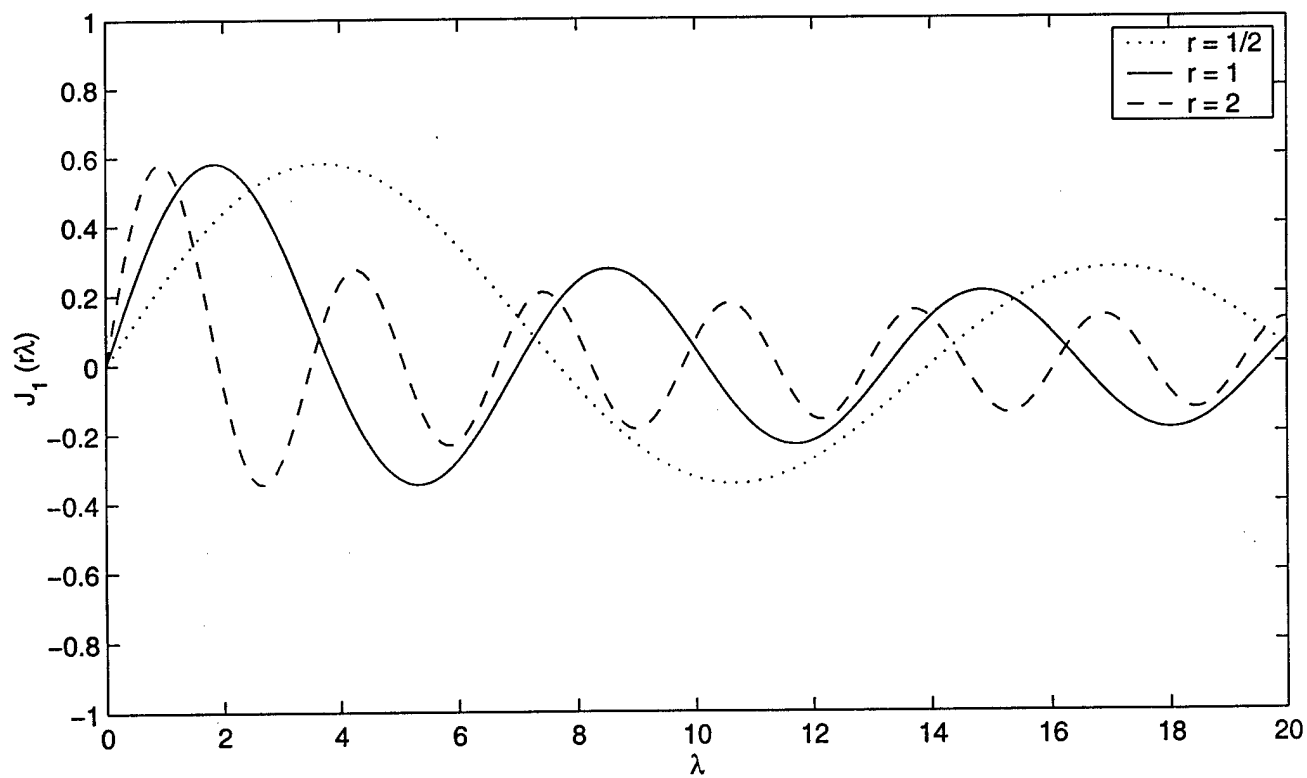
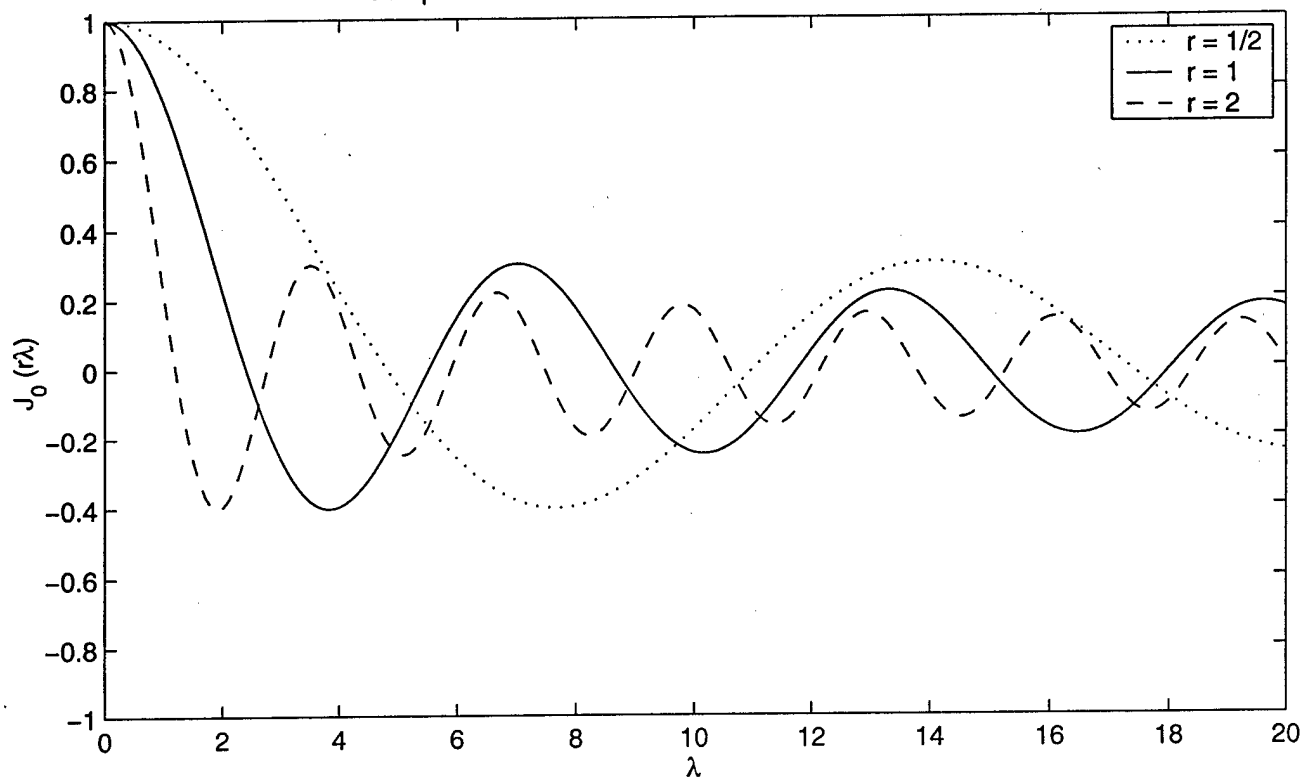


Figure 17

Comparison of Scaled Bessel Functions of the First Kind



```

%
% Matlab m-file to take the derivative of a geoid height
% profile and compare a first difference derivative to the
% FFT derivative approach.
%
% The file geosatd.dat is loaded.
% The first column of the file is time (not used here).
% The second column of the file is latitude in degrees.
% The third column of the file is longitude in degrees.
% The fourth column is geoid height in meters.
% The fifth column is gravity anomaly in milligals.
% The sixth column is uncertainty in gravity anomaly.
% (note this is a descending track so latitude decreases
% with increasing time.)
%
% There are 512 evenly spaced points. The total length of the
% profile is 1705000 m.
%
% Get the hw1part.m file and the data file using fetch or ftp
% baltica.ucsd.edu
% cd pub/class/hw1
% mget *
%
% load geosatd.dat
% lat=geosatd(:,2);
% lon=geosatd(:,3);
% geoid=geosatd(:,4);
%
% remove the mean and window the profile to minimize edge effects
%
% nx=length(lat);
% window=hanning(nx);
% geoid=(geoid-mean(geoid)).*window;
%
% plot geoid height
%
% subplot(2,1,1), plot(lat,geoid);
% ylabel('geoid height (m)')
%
% get the profile length and data spacing
%
% L=1705000.;
% dx=L/nx;
%
% compute the derivative using the first difference formula.
% multiply the dimensionless slope by 1e06 to get microradians.
% duplicate the last point to extend the length from 511 to 512.
% note there is a shift
%
vd = 1.e6*diff(geoid)/dx;
nd = length(vd);
vd = [vd;vd(nd:nd)];
%
% now compute the derivative using the derivative property.
% first compute FFT and do an fftshift to make it easy to generate
% wavenumbers.
%
cg = fftshift(fft(geoid));
%
% generate the wavenumber. if these wavenumbers are wrong the

```